Volume 1 | Number 1 | Jan 2013 | Pages 1–100

Journal of
Materials Chemistry A

Materials for energy and sustainability
www.rsc.org/materialsA

Li⁺

ROYAL SOCIETY
OF CHEMISTRY

ROYAL SOCIETY
OF **CHEMISTRY**

www.rsc.org/materialsA

Solvothermal Synthesis of ZnO-Decorated α-Fe$_2$O$_3$ Nanorods with Highly Enhanced Gas-Sensing Performance toward n-Butanol

Yusuf V. Kaneti[a], Quadir M.D. Zakaria[a], Zhengjie Zhang, Chuyang Chen[a], Jeffrey Yue[b],

Minsu Liu[a,] Xuchuan Jiang[a,]*and Aibing Yu[a]

[a]*School of Materials Science and Engineering, The University of New South Wales, Sydney NSW 2052, Australia*

[b]*Department of Chemical Engineering, University College London, Torrington Place, London WC1E 7JE, United Kingdom.*

Abstract

This paper reports a newly-developed solvothermal strategy for the synthesis of ZnO-decorated α-Fe$_2$O$_3$ nanorods based on the reaction of α-Fe$_2$O$_3$ nanorods with zinc sulfate and urea in autoclaves at 180 °C. The resulted nanocomposites consist of porous α-Fe$_2$O$_3$ nanorods with diameters of 100-200 nm, surface decorated with small ZnO nanoparticles (10-20 nm). The ZnO NPs are found to grow epitaxially on {110} planes of α-Fe$_2$O$_3$, forming an interfacial orientation relationship of (100)$_{ZnO}$/(110)$_{α-Fe_2O_3}$. The addition of ZnO is found to shift the Fe 2p peak position in the α-Fe$_2$O$_3$/ZnO nanocomposites to higher binding energies due to the formation of the α-Fe$_2$O$_3$/ZnO heterojunction interface. The gas-sensing results show that the ZnO-decorated α-Fe$_2$O$_3$ nanorods exhibit excellent sensitivity selectivity, and stability toward n-butanol gas at a low optimum temperature of 225 °C. In particular, they show higher sensitivity compared to pure α-Fe$_2$O$_3$ (4 times higher) and ZnO nanorods (2.5 times higher), respectively, along with faster response times. The significant enhancement in sensitivity may be attributed to the chemical and electronic sensitization induced by the ZnO nanoparticles deposited on the surfaces of the α-

Fe_2O_3 nanorods. The findings reported in this study will be useful for the design and construction of surface modified-metal oxide nanostructures with enhanced gas-sensing performance.

Keywords: iron oxide, zinc oxide, nanocomposites, n-butanol, sensitivity, gas sensing, nanorods

1. Introduction

Hetero-nanostructures consisting of two or more metal oxides have attracted increasing attention due to the possibilities of integrating the physical and chemical properties of these oxides. To date, many different metal oxide nanocomposites have been reported, including α-Fe_2O_3@SnO_2 nanorattles[1], ZnO-SnO_2 nanofibres[2], SnO_2@CuO core-shell nanorods[3], and ZnO-TiO_2 nanofibres.[4] These nanocomposites have shown enhanced properties and functionalities compared to their individual metal oxide counterparts in applications such as photocatalysis,[5, 6] gas-sensors,[7, 8] and lithium-ion batteries.[9, 10]

Hematite (α-Fe_2O_3), an *n*-type semiconductor with band-gap (E_g) of 2.1 eV, is particularly attractive for gas-sensing applications due to its high chemical stability, low manufacturing cost, low toxicity and high resistance to corrosion. Various α-Fe_2O_3 nanostructures (nanotubes,[11] nanospheres,[12] and nanowires[13]) have shown good sensitivity and/or selectivity toward various volatile and toxic gases, such as H_2S, acetic acid and ethanol. To further enhance the sensitivity and selectivity, surface modification of the α-Fe_2O_3 nanomaterials with noble metals (e.g., Ag,[14] Au[15]) or other metal oxides such as TiO_2[16] and SnO_2[17] have been proposed. Zinc oxide (ZnO) is particularly attractive as an additive due to its low cost, good thermal stability, and high mobility of conduction electrons.[18, 19] For example, Zhang et al.[18] prepared α-Fe_2O_3@ZnO core-shell nanospindles by multiple-step dip-coating of the α-Fe_2O_3 nanospindles in zinc acetate solution,

followed by annealing at 350 °C for 2 h. Wu et al.[19] reported a seed-mediated synthesis of α-Fe_2O_3@ZnO core-shell nanoshuttles by heating the α-Fe_2O_3 nanoshuttles in a basic solution containing zinc acetate, followed by calcination at 550 °C for 2 h. Despite some success, previous methods to synthesize α-Fe_2O_3/ZnO nanocomposites have suffered from the following limitations, including (i) the use of multiple seeding steps and (ii) the need for high-temperature treatment ($\geq$ 350 °C), and (iii) the complete enclosure of the α-Fe_2O_3 core by the ZnO shell, which reduced the adsorption of oxygen molecules on the surface of the α-Fe_2O_3, leading to a reduction in sensitivity.[18, 19] This is because the sensitivity of a metal oxide gas sensor is greatly dependent on the amount of chemisorbed oxygen on the surface of the oxide material.[20] Therefore, it is important to develop a simple and effective fabrication method for the synthesis of α-Fe_2O_3/ZnO nanocomposites with highly accessible surfaces for gas adsorption. Furthermore, in these reports,[18, 19] the growth mechanism of the ZnO nanoparticles on the α-Fe_2O_3 substrate and the influence of the Zn content on the gas-sensing properties of the α-Fe_2O_3 nanorods were not investigated.

This work demonstrates a facile and efficient strategy for the fabrication of ZnO-decorated α-Fe_2O_3 nanostructures through the solvothermal reaction of α-Fe_2O_3 nanorods with zinc sulfate and urea under mild reaction conditions. The morphology and composition of the products have been characterized by X-ray diffraction (XRD), scanning electron microscopy (SEM), transmission electron microscopy (TEM), X-ray photoelectron spectroscopy (XPS), and energy dispersive spectroscopy (EDS). The formation and growth mechanisms of the ZnO NPs on the surfaces of the α-Fe_2O_3 nanorods are discussed and the influence of the Zn content on the gas-sensing performance of the α-Fe_2O_3/ZnO products has been investigated. The gas-sensing properties such as sensitivity, selectivity, stability and response-recovery behaviors have been

evaluated, and the possible gas-sensing mechanism is discussed. The findings will be useful for the design of metal oxide nanocomposites for applications such as gas sensors and catalysts.

2. Experimental Section

2.1. Chemicals

Iron(III) chloride hexahydrate ($FeCl_3.6H_2O$, 97%), zinc sulfate heptahydrate ($ZnSO_4.7H_2O$, 99.9%), zinc chloride ($ZnCl_2$, 99%), sodium hydroxide (NaOH, 99%), urea ($CO(NH_2)_2$, 99%), 1-methyl-2-pyrrolidinone (C_5H_9NO, 99.5%), polyvinylidene fluoride ($(CH_2CF_2)_n$, 99.5%), methanol (CH_4, 99%), ethanol (C_2H_6O, 95%), absolute ethanol (C_2H_6O, 99.9%), n-butanol ($C_4H_{10}O$, 99%), formaldehyde (HCHO, 37.5 wt% in H_2O), and acetone (C_3H_6O, 99.9%) were purchased from Sigma Aldrich and used as received without further purification. Ultra-pure water was used in all the synthesis processes.

2.2. Synthesis

2.2.1. Synthesis of porous α-Fe₂O₃ nanorods

In a typical procedure, 6.758 g of $FeCl_3.6H_2O$ was dissolved in 250 mL of distilled water to make a 0.1 M $FeCl_3.6H_2O$ solution. This solution was subsequently heated at 80 ⁰C for 16 h to obtain akaganeite (β-FeOOH) nanorods. These nanorods were then collected by centrifugation and thoroughly washed with deionized water and 1.0 M NaOH solution several times to remove excess chlorine (Cl⁻) ions and finally dried at 60 ⁰C for 5 h. Upon drying, the β-FeOOH nanorods were calcined in air at 400 ⁰C for 2 h to convert them to porous α-Fe₂O₃ nanorods.

2.2.2. Synthesis of ZnO nanorods

In a typical procedure, a 0.05 M $ZnCl_2$ solution was first prepared by dissolving 0.0682 g of $ZnCl_2$ salt in 10 mL of water. In a separate beaker, 0.024 g of NaOH pellets was dissolved in 40 mL of water to form a 0.15 M NaOH solution. Then, 2 mL of 0.05 M $ZnCl_2$ solution was added to the 0.15 M NaOH solution and rapidly stirred for 15 minutes to produce a white-colored suspension. Finally, this suspension was transferred to a 50 mL Teflon-lined stainless steel autoclave, sealed and heated at 150 °C for 16 h. The obtained white precipitates were then collected by centrifugation and thoroughly washed with deionized water and ethanol several times and finally dried at 60 °C for 5 h.

2.2.3. Synthesis of ZnO-decorated α-Fe_2O_3 nanorods

In a typical protocol, 0.0359 g of $ZnSO_4.7H_2O$ and 0.036 g of $CO(NH_2)_2$ were first dissolved in 20 mL of a water/ethanol (95% purity) mixture (water/ethanol = 5:3) until a clear solution is achieved. Secondly, 0.032 g of porous α-Fe_2O_3 nanorods was well sonicated into the above mixture and then stirred for 15-20 minutes. Finally, this solution was transferred to a 50 mL Teflon-lined stainless steel autoclave. The autoclave was sealed and heated at 180 °C for 24 h and then cooled to room temperature naturally. The reddish-brown product was collected by centrifugation and washed with deionized water and ethanol several times and finally dried at 60 °C for 6 h. To investigate the effect of the Zn content on the gas sensing properties, a series of α-Fe_2O_3/ZnO samples were prepared by using different amounts of the $ZnSO_4.7H_2O$, i.e. 0.0036 g (S1), 0.0180 g (S2), 0.0269 g (S3) and 0.036 g (S4), with other parameters such as the concentration of urea, the amount of α-Fe_2O_3 nanorods, the reaction temperature and the reaction time kept constant.

2.3. Characterization

The phase composition and purity of the α-Fe$_2$O$_3$/ZnO nanocomposites were examined using Phillips X'pert Multipurpose X-Ray Diffraction System (MPD) with Cu Kα radiation (λ = 1.54 Å) operated at 40 kV and 40 mA, in the 2θ range of 20-70°, with a step size of 0.02°. Scanning electron microscopy (SEM) analysis was performed using a FEI Nova NanoSEM 230 field emission scanning electron microscope. The transmission electron microscopy (TEM) images were obtained using a Tecnai G^2 20 transmission electron microscope operated at an accelerating voltage of 200 kV. High resolution transmission electron microscopy (HRTEM) images were recorded on a Phillips CM200 field emission gun transmission electron microscope with an accelerating voltage of 200 kV. The surface analysis of the ZnO-decorated α-Fe$_2$O$_3$ nanorods were carried out using an ESCALAB250Xi X-ray photoelectron spectrometer, using Al-Kα radiation as the excitation source. The Brunauer–Emmett–Teller (BET) surface area and pore size distribution of the products were obtained from nitrogen physisorption isotherms (adsorption–desorption branches) at 77 K on a Micromeritics Tristar 3000 instrument. Prior to the BET measurement, the samples were degassed overnight under vacuum at 150 °C to vaporize water molecules adsorbed on the materials.

2.4. Gas sensor fabrication and measurement

The gas sensor was built as follows: firstly, the α-Fe$_2$O$_3$/ZnO nanocomposites were mixed and ground with the binder polyvinylidene fluoride (PVDF) in an agate mortar. Secondly, the solvent 1-methyl-2-pyrollidone was added into this mixture to form brownish-red slurry, which was subsequently coated on a ceramic tube with previously printed gold (Au) electrodes and platinum (Pt) conducting wires. Finally the ceramic tube was sintered at 450 ºC for 3 h to enhance the stability of the sensor. The gas-sensing properties of the α-Fe$_2$O$_3$/ZnO nanocomposites were

tested using a computer-controlled WS-30A gas-sensing measurement system, as shown in Fig. S1 (see ESI).

Prior to the test, a Ni-Cr resistor was inserted into the ceramic tube as a heater, which allows for the control of the working temperature by adjusting the heating voltage ($V_{heating}$). A reference resistor was placed in series with the sensor to form a complete measurement circuit. The test gas was injected into the testing chamber using a micro-syringe. The sensitivity of the sensor (S) is defined as the ratio of the resistances measured in air (R_a) and in the tested gas atmosphere (R_g): $S= R_a/R_g$. The output voltage was fixed at 5 V and the relative humidity was between 50-65%. The response time (τ_{res}) is defined as the time required by the sensor to achieve 90% of its maximum response after the gas injection, whereas the recovery time (τ_{res}) is the time taken by the sensor to reach 10% of its initial resistance after removal of the gas. For comparison, sensors were also prepared from the pure α-Fe$_2$O$_3$ and ZnO nanorods, using similar procedures as described previously. Digital photographs of the as-prepared sensors are provided in Fig. S2.

3. Results and discussion

3.1 Composition and morphology

Fig. 1 compares the XRD patterns of pure α-Fe$_2$O$_3$ and ZnO nanorods, and α-Fe$_2$O$_3$/ZnO nanocomposites. As shown in Fig. 1a and c, the XRD patterns of the as-prepared α-Fe$_2$O$_3$ and ZnO nanorods clearly shows all the diffraction peaks of rhombohedral α-Fe$_2$O$_3$ (JCPDS No. 33-0644) and hexagonal wurtzite ZnO (JCPDS No. 36-1451), respectively. The XRD pattern of the achieved nanocomposites (Fig. 1b) contains the peaks of both α-Fe$_2$O$_3$ and ZnO. No other peaks related to impurities are observed, which indicates the high purity of the product.

Fig. 2a and b show the SEM and TEM images of the α-Fe$_2$O$_3$ nanorods, respectively, prior to the

coating process. These nanorods have diameters in the range of 100-200 nm, and their surfaces

are relatively smooth prior to the ZnO deposition. The EDS spectrum of the α-Fe$_2$O$_3$ nanorods

(Fig. 2c) confirms the presence of both elemental Fe and O. Furthermore, the TEM image in Fig.

3a clearly indicates the highly porous nature of the synthesized α-Fe$_2$O$_3$ nanorods. These pores

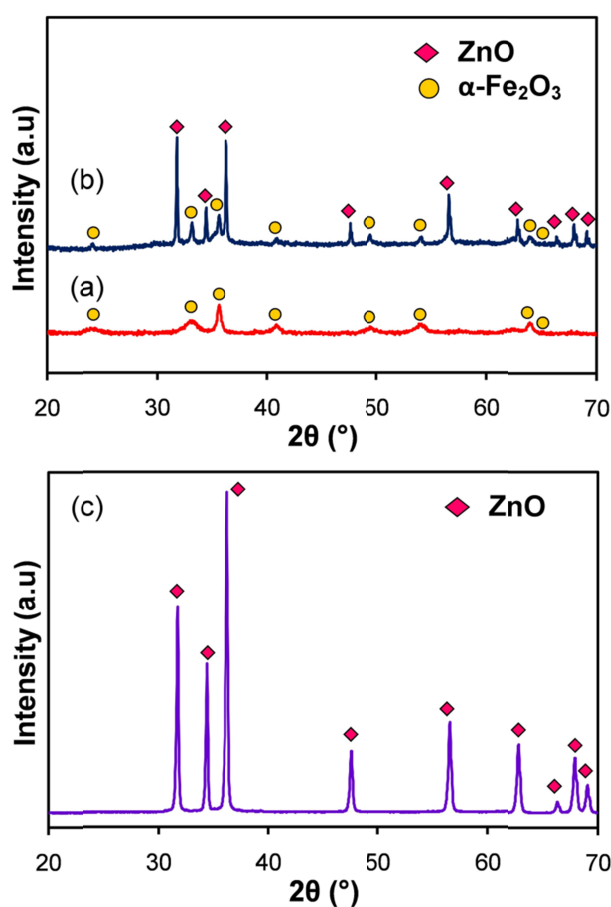originate from the dehydroxilation of β-FeOOH nanorods during the calcination process.[21]

Fig. 1 XRD patterns of (a) pure α-Fe$_2$O$_3$ nanorods, (b) ZnO-decorated α-Fe$_2$O$_3$ nanorods, and (c)

pure ZnO nanorods.

After coating, the surfaces of the α-Fe$_2$O$_3$ nanorods become noticeably rougher as they are

decorated with numerous ZnO NPs, as shown in Fig. 2d and e. The EDS spectrum of the ZnO-

decorated α-Fe₂O₃ nanorods (Fig. 2f) clearly indicates the presence of Zn peaks, in addition to

the Fe and O peaks. The morphology of the as-prepared ZnO nanorods was also investigated

using SEM and TEM techniques as shown in Fig. 2g and h, respectively. The diameter of the

obtained ZnO nanorods varies from 100-200 nm, and the surfaces of these ZnO nanorods are

relatively smooth. The EDS spectrum of the ZnO nanorods proves the existence of both Zn and
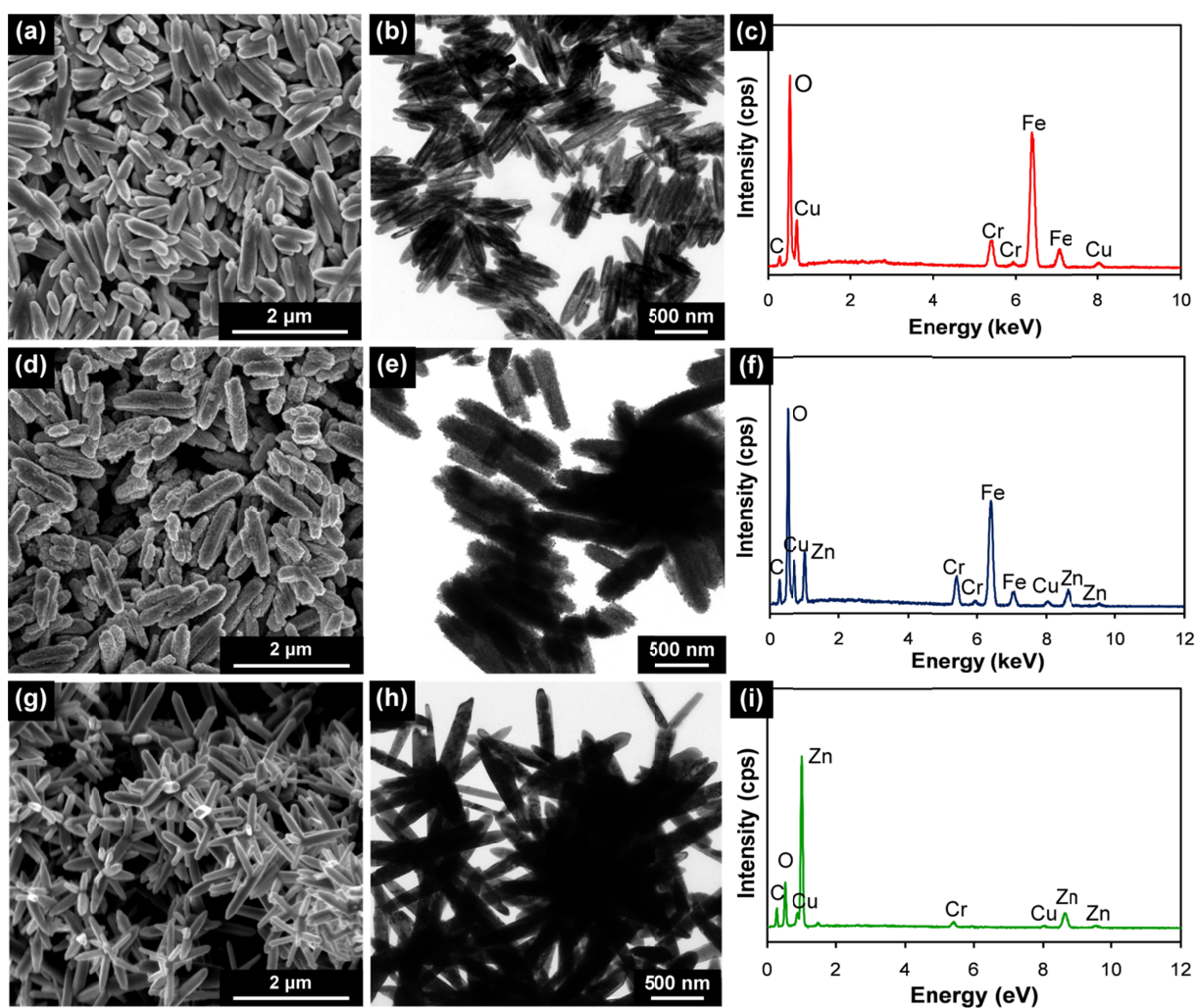
O elements, as shown in Fig. 2i.

Fig. 2 SEM and TEM images and EDS analysis of (a, b, c) pure α-Fe₂O₃ nanorods, (d, e, f) ZnO-

decorated α-Fe₂O₃ nanorods, and (g, h, i) pure ZnO nanorods.

To gain further insights into the crystallographic features of the pure α-Fe$_2$O$_3$ and ZnO nanorods as well as the ZnO-decorated α-Fe$_2$O$_3$ nanorods, HRTEM and the associated diffraction techniques were employed. The HRTEM analysis of a single α-Fe$_2$O$_3$ nanorod (Fig. 3b) reveals three groups of lattice fringes, each with a *d*-spacing of 0.252 nm, which corresponds to the *d*-spacing of (110), ($\bar{1}$20) and ($\bar{2}$10) planes of α-Fe$_2$O$_3$, respectively. The lateral growth direction of the α-Fe$_2$O$_3$ nanorods is [110], as indicated in Fig. 3b. The corresponding selected area diffraction (SAED) pattern of the α-Fe$_2$O$_3$ nanorods (Fig. 3c) reveals a diffraction pattern which can be indexed to the [001] zone axis of rhombohedral α-Fe$_2$O$_3$.
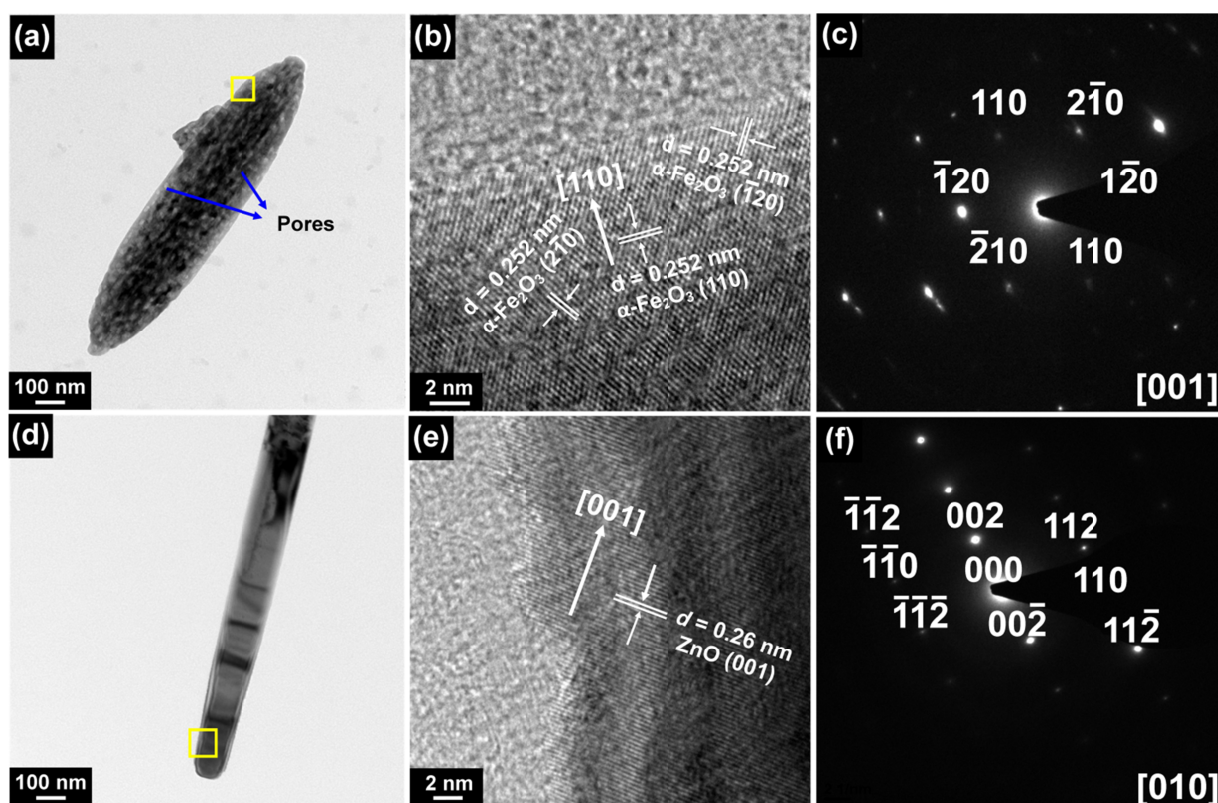

Fig. 3 TEM, HRTEM, and SAED images of (a, b, c) porous α-Fe$_2$O$_3$ nanorods and (d, e, f) ZnO nanorods.

Similar HRTEM and diffraction analysis were also conducted following the ZnO decoration on

the α-Fe$_2$O$_3$ nanorods. Fig. 4a and b shows the TEM images of a single α-Fe$_2$O$_3$ nanorod with

many small ZnO NPs deposited on its surface. The rectangular area at the edge of the α-Fe$_2$O$_3$

particle in Fig. 4b is magnified in Fig. 4d to highlight the lattice fringes. The d-spacing between

adjacent lattice fringes in the α-Fe$_2$O$_3$ nanorod is ~0.257 nm, which corresponds well to the (110)

plane of α-Fe$_2$O$_3$. The d-spacing between the adjacent lattice fringes of the ZnO NP is ~0.285

nm, which can be well indexed to the (100) plane of ZnO.

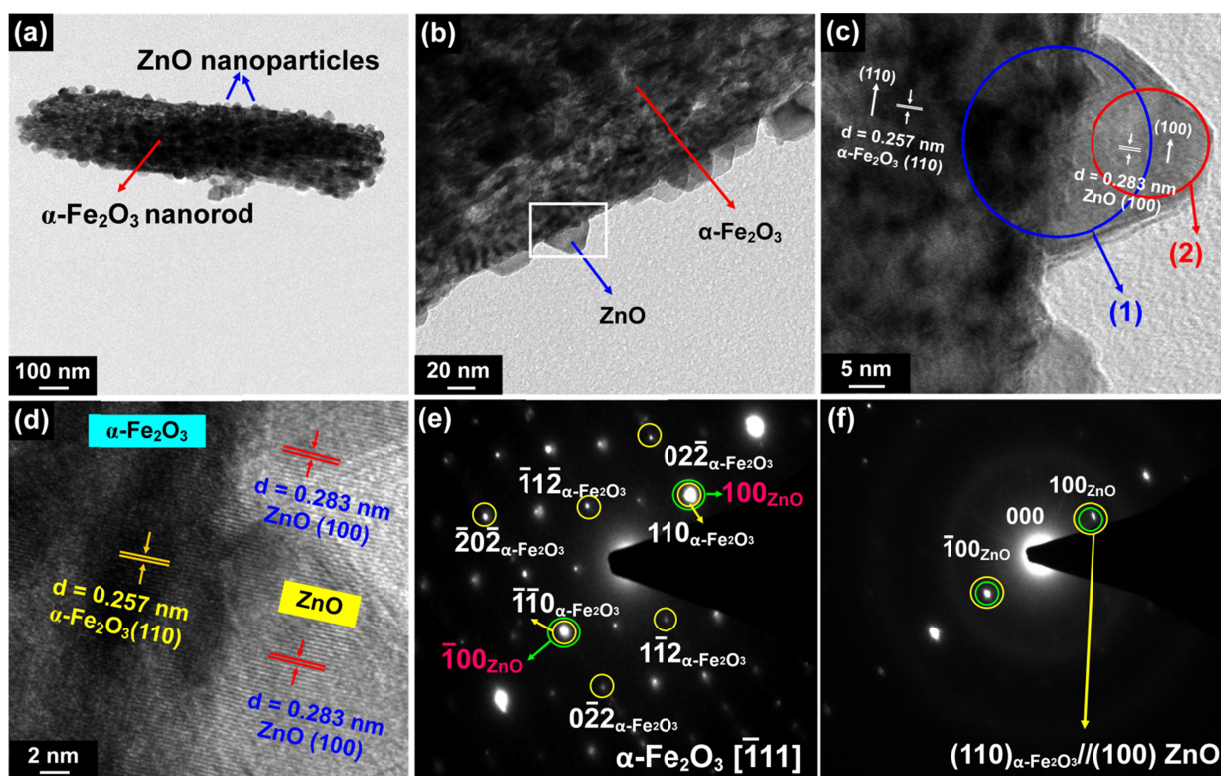**Fig. 4** (a, b) Bright field TEM and (c, d) HRTEM images of the ZnO-decorated α-Fe$_2$O$_3$

nanorods. SAED patterns of the encircled area in 1 and 2 in Fig. c are shown in (e) combination

of α-Fe$_2$O$_3$ (at [111] zone axis) and ZnO and (f) of the single ZnO NP, respectively.

The lattice information conform to the corresponding SAED patterns in Fig. 4e and f. Using the

smallest aperture of the TEM, the SAED pattern in Fig. 4e covers both α-Fe$_2$O$_3$ nanorod and

ZnO NP within the schematic circle 1 in Fig. 4c. Likewise, the SAED pattern in Fig. 4f is taken exclusively from the ZnO NP within the schematic circle 2 in Fig.4c. Therefore, the SAED in Fig. 4e combines both α-Fe$_2$O$_3$ nanorod and ZnO NP, and the SAED pattern in Fig. 4f is only from the ZnO NP alone. Indexing of the SAED pattern in Fig. 4e shows that the (110) and ($\bar{1}\bar{1}$0) planes of the α-Fe$_2$O$_3$ nanorod coincides with the (100) and ($\bar{1}$00) planes of ZnO NP, respectively. Being consistent with the SAED, the HRTEM image in Fig. 4d reveals that the (100) planes of ZnO are stacked parallel to the (110) planes of α-Fe$_2$O$_3$, forming an interfacial orientation relationship of (110)$_{\alpha\text{-Fe2O3}}$//(100)$_{ZnO}$. The deposited ZnO NPs are found to preferentially grow along the [100]$_{ZnO}$ direction as supported by the strong relative intensity of the ZnO(100) peak (at 2θ= 38°) in the XRD pattern of the ZnO-decorated α-Fe$_2$O$_3$/ZnO nanorods (Fig. 1b).[22]

Importantly, it is noted in Fig. 4e that the (110) and ($\bar{1}\bar{1}$0) diffraction spots of α-Fe$_2$O$_3$ overlap the (100) and ($\bar{1}$00) diffraction spots of ZnO, respectively, in the axial direction, which implies the good lattice compatibility between these two lattice planes ((110)$_{\alpha\text{-Fe2O3}}$ and (100)$_{ZnO}$). Such overlapping has also been previously observed in the case of α-Fe$_2$O$_3$/SnO$_2$ hierarchical heterostructures where the (110) diffraction spot of α-Fe$_2$O$_3$ overlapped with the (200) diffraction spot of SnO$_2$.[6] The HRTEM and SAED results therefore prove that the interfacial orientation relationship is (110)$_{\alpha\text{-Fe2O3}}$//(100)$_{ZnO}$. The HRTEM image of the ZnO nanorods shown in Fig. 3e reveals clear lattice fringes with a *d*-spacing of 0.26 nm, indexed to the *d*-spacing of (001) plane of ZnO, implying the [001] growth direction of the ZnO nanorods.
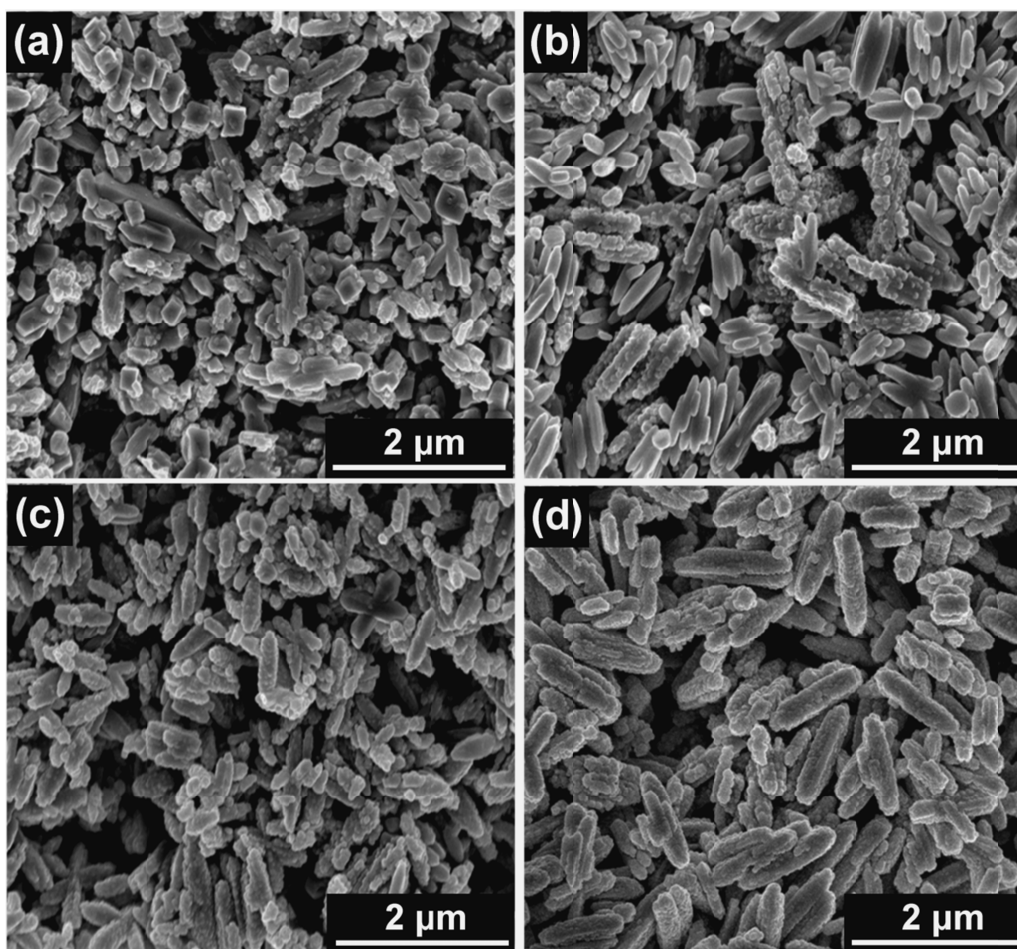
Fig. 5 SEM images of α-Fe_2O_3/ZnO products obtained with different amounts of Zn precursor ($ZnSO_4.7H_2O$): (a) 0.0036 g (S1), (b) 0.018 g (S2), (c) 0.0269 g (S3), and (d) 0.0359 g (S4).

The influence of the Zn precursor concentration on the morphology of the obtained α-Fe_2O_3/ZnO products is shown in Fig. 5 and S4. It is evident from Fig. 5a and S4a that when a low amount of Zn precursor (0.0036 g) is used (S1), only few ZnO NPs are coated onto the nanorods and a number of the α-Fe_2O_3 nanorods disassemble into irregular box like-structures. This may be caused by the presence of insufficient amounts of Zn^{2+} ions (due to the low concentration of the Zn precursor) in the solution to react with OH^- ions released by urea at 180 °C. This subsequently results in the destruction of the α-Fe_2O_3 nanorods as a result of highly basic

environment. When the quantity of $ZnSO_4$ is gradually increased from 0.018 (S2) to 0.036 g (S4), increasing density and more uniform coverage of ZnO NPs are observed on the surfaces of the nanorods, with the best result achieved at a Zn precursor amount of 0.036 g (S4). The particle size of the ZnO NPs in these samples is similar, with the size ranging from 10 to 20 nm.

XPS analysis was used to obtain further information regarding the surface structure and composition of the α-Fe_2O_3, ZnO and α-Fe_2O_3/ZnO products, as shown in Table 1 and Fig. 6. The XPS quantitative results reveal that the Zn atomic% of samples S1, S2, S3, and S4 are 3.27, 12.7, 14.6, and 17.0 at%, respectively. It is clear from Table 1 that with increasing amounts of Zn, the atomic% of Fe gradually decreases, indicating the increasing coverage of the surfaces of the α-Fe_2O_3 nanorods by the ZnO NPs.

Table 1 XPS quantitative analysis of the α-Fe_2O_3, ZnO and α-Fe_2O_3/ZnO products

Sample	Fe (at %)	Zn (at %)	O (at %)
α-Fe_2O_3 nanorods	35.8	0	53.2
α-Fe_2O_3/ZnO (S1)	25.3	3.27	56.6
α-Fe_2O_3/ZnO (S2)	22.1	12.7	56.4
α-Fe_2O_3/ZnO (S3)	20.4	14.6	56.4
α-Fe_2O_3/ZnO (S4)	18.3	17.0	56.7
ZnO nanorods	0	49.2	47.7

Fig. 6a displays the high resolution spectra of Fe species in pure α-Fe_2O_3 and α-Fe_2O_3/ZnO samples containing varying amounts of Zn. In the pure α-Fe_2O_3 nanorods, the peaks at 710.68 eV and 724.28 eV can be ascribed to the peaks of Fe $2p_{3/2}$ and Fe $2p_{1/2}$, respectively, and the

presence of the Fe 2p satellite peak at ~719 eV confirms the Fe^{3+} state of the iron oxide product. However after ZnO modification, the intensities of the Fe 2p peaks are reduced and their positions are gradually shifted to higher binding energies with increasing Zn content, with the positions of Fe $2p_{3/2}$ and Fe $2p_{1/2}$ shifting to 711.28 and 724.98 eV, respectively, at 17.0 at% Zn (sample S4). These observations suggest the slight alteration of Fe electronic structure due to the formation of α-Fe_2O_3/ZnO heterojunction interface which plays an important role in the gas-sensing mechanism of the nanocomposites.[18] Despite the shift, the locations of the Fe 2p satellite peaks in the α-Fe_2O_3/ZnO samples remain more or less the same, indicating that the Fe remains in a 3+ valence state.

The high resolution spectra of the Zn species in the α-Fe_2O_3/ZnO products (Fig. 6b) show a strong peak at 1021.48 eV for sample S1, 1021.38 eV for sample S2, 1021.58 eV for sample S3, and 1021.68 eV for sample S4, which can be indexed to the Zn $2p_{3/2}$ peak, corresponding to Zn^{2+} bonded to O in ZnO. Moreover, it can be observed from Fig. 6b that the intensities of the Zn 2p peaks clearly rises with increasing Zn content in the α-Fe_2O_3/ZnO product, which corresponds to the increase in the amount of ZnO NPs decorated on the surfaces of the α-Fe_2O_3 nanorods. For pure ZnO nanorods, the Zn 2p peak is located at a slightly lower binding energy of 1021.28 eV. The deconvolution of the O 1s peak of a typical α-Fe_2O_3/ZnO composite material (Fig. 6c) reveals the existence of three oxygen species: the peaks at 529.88 eV and 531.68 eV correspond to M-O and M-OH bonds, respectively (M= Fe or Zn), and the peak at 532.58 eV corresponds to the presence of different M-OH bonds or chemisorbed water.[18]
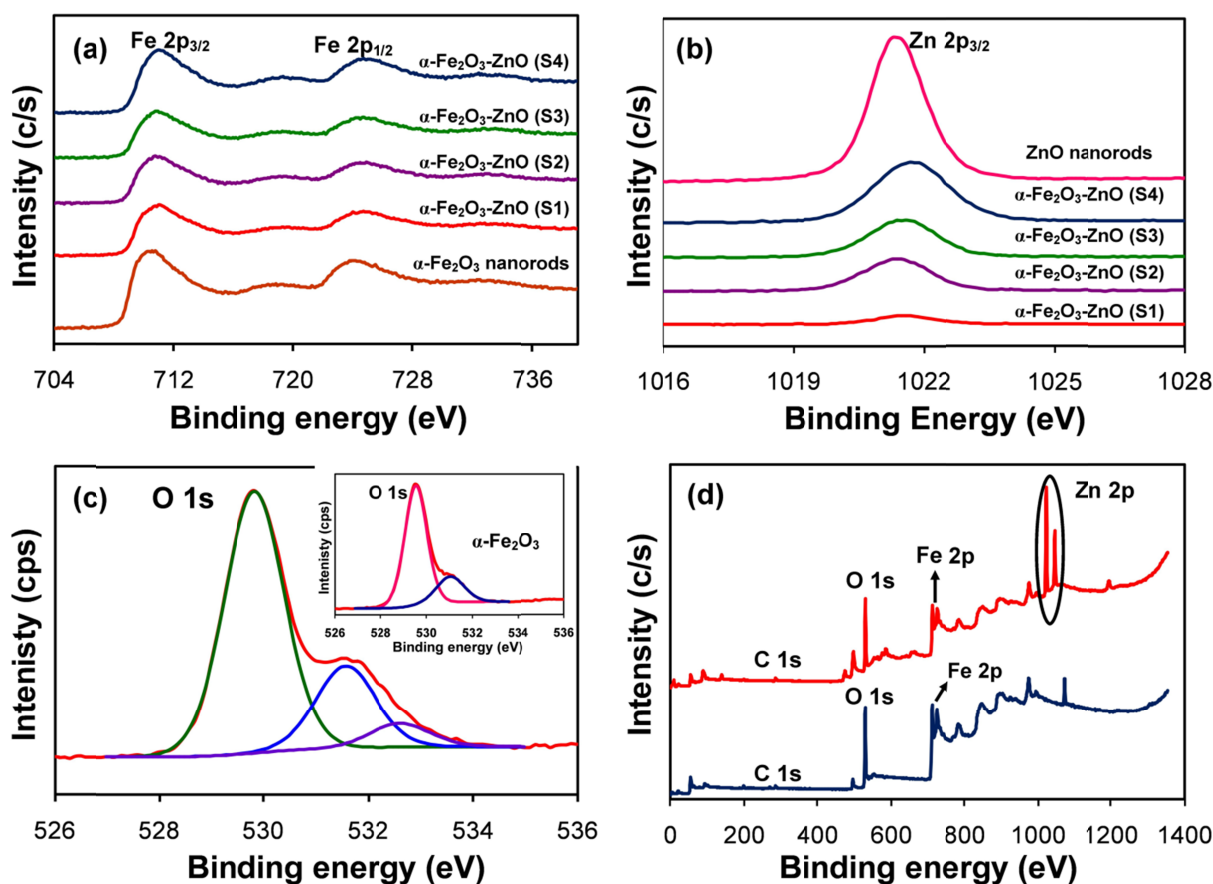
Fig. 6 (a) Fe 2p XPS peaks of pure α-Fe$_2$O$_3$ and α-Fe$_2$O$_3$/ZnO products containing different amounts of Zn, (b) Zn 2p peaks of ZnO nanorods and α-Fe$_2$O$_3$/ZnO nanocomposites containing various amounts of Zn and, (c) comparison of O 1s XPS peaks of pure α-Fe$_2$O$_3$ (inset) and ZnO-decorated α-Fe$_2$O$_3$ nanorods, and (d) survey spectra of pure α-Fe$_2$O$_3$ (blue) and ZnO-decorated α-Fe$_2$O$_3$ nanorods (red).

BET analysis was also carried out to further confirm the highly porous nature of the as-prepared α-Fe$_2$O$_3$ nanorods and ZnO-decorated α-Fe$_2$O$_3$ nanorods. Fig. S5a and b show the N$_2$ adsorption-desorption isotherms and Barret-Joyner-Halenda (BJH) pore size distribution plot of the as-prepared α-Fe$_2$O$_3$ nanorods. Based on the IUPAC classification, the isotherm can be ascribed to a type IV isotherm with a type H3 hysteresis loop in the P/P_0 range of ~0.4-0.9. The BJH

distribution plot shown in Figure S5b shows the presence of a primary pore size distribution peak centered at ~2.5 nm and a secondary distribution peak centered at ~8 nm. These results indicate the mesoporous nature of the as-prepared α-Fe$_2$O$_3$ nanorods. The BET surface area of the as-synthesized α-Fe$_2$O$_3$ nanorods is measured to be 60.86 m^2/g. In comparison, The BET surface area of the ZnO-decorated α-Fe$_2$O$_3$ nanorods (sample S4) is slightly lower (~44 m^2/g), because of the slight increase in the size of the α-Fe$_2$O$_3$ nanorods following the ZnO coating process (Figure S5c). Similar to the pure α-Fe$_2$O$_3$ nanorods, the isotherm of the ZnO-decorated α-Fe$_2$O$_3$ nanorods can also be indexed to a type IV isotherm with a type H3 hysteresis loop in the P/P_0 range of ~0.4-0.95. The BJH pore distribution plot of the ZnO-decorated α-Fe$_2$O$_3$ nanorods depicted in Figure S5d reveals the existence of a primary pore size distribution peak centered at ~2.2 nm and a secondary distribution peak centered at ~7 nm, which confirms their mesoporous nature.

3.2 Formation mechanism

The formation mechanism of the ZnO NPs on the surfaces of the α-Fe$_2$O$_3$ nanorods can be explained as follows. Firstly, the Zn precursor, ZnSO$_4$, dissolves in the water/ethanol solvent to produce Zn^{2+} ions:

$$ZnSO_4 \rightarrow Zn^{2+} + SO_4^{2-} \tag{1}$$

At high temperatures ($\geq$ 140°C), the hydrolysis of urea occurs, generating OH$^-$ ions in the solution, which in turn increases the basicity of the solution:[23]

$$CO(NH_2)_2 + H_2O \rightarrow 2NH_3 + CO_2\uparrow \tag{2}$$

$$NH_3 + H_2O \rightarrow NH_4^+ + OH^- \tag{3}$$
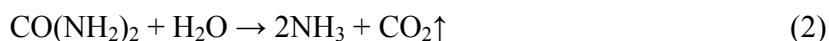
The Zn^{2+} ions then react with the OH$^-$ ions produced by the hydrolysis of urea to form zinc hydroxide, Zn(OH)$_2$:

$$Zn^{2+} + 2OH^- \rightarrow Zn(OH)_2 \qquad (4)$$

After a prolonged heating period, the zinc hydroxide decomposes and forms ZnO according to

Eq. 5:

$$Zn(OH)_2 \xrightarrow{\Delta} ZnO \qquad (5)$$

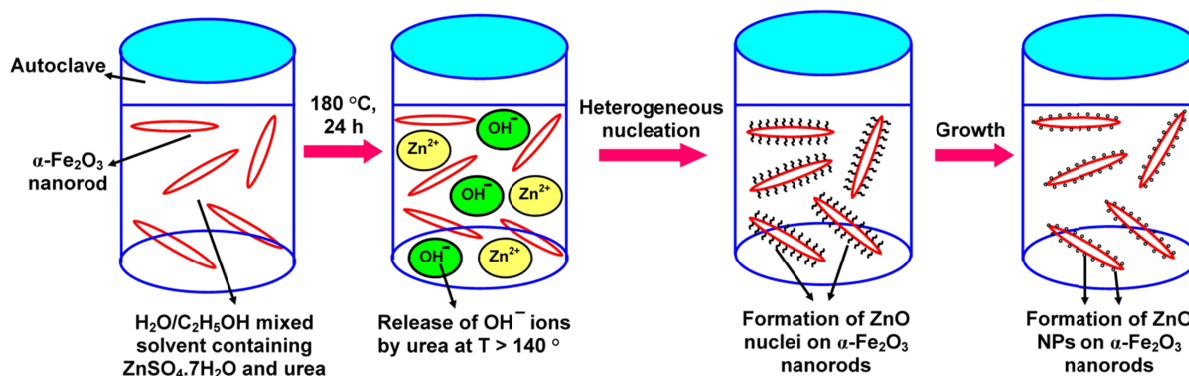**Fig. 7** Schematic diagram illustrating the formation of ZnO NPs on the surfaces of α-Fe$_2$O$_3$ nanorods.

Previously, our simulation study has shown that the interaction energies of Ag, Pt or Pd NPs are

much higher when deposited on a porous surface of α-Fe$_2$O$_3$ relative to a smooth one, resulting

in easier depositions on the α-Fe$_2$O$_3$ surface.[24] In the current reaction system, the as-prepared α-

Fe$_2$O$_3$ nanorods are highly porous in nature and therefore the total potential energy of the ZnO

NPs can also be significantly decreased when deposited on such porous surfaces. Hence, the ZnO

NPs are more likely to nucleate and grow on the surfaces of the α-Fe$_2$O$_3$ nanorods (Fig. 7) via

heterogeneous nucleation rather than forming separate nuclei by homogenous nucleation during

the synthesis process.
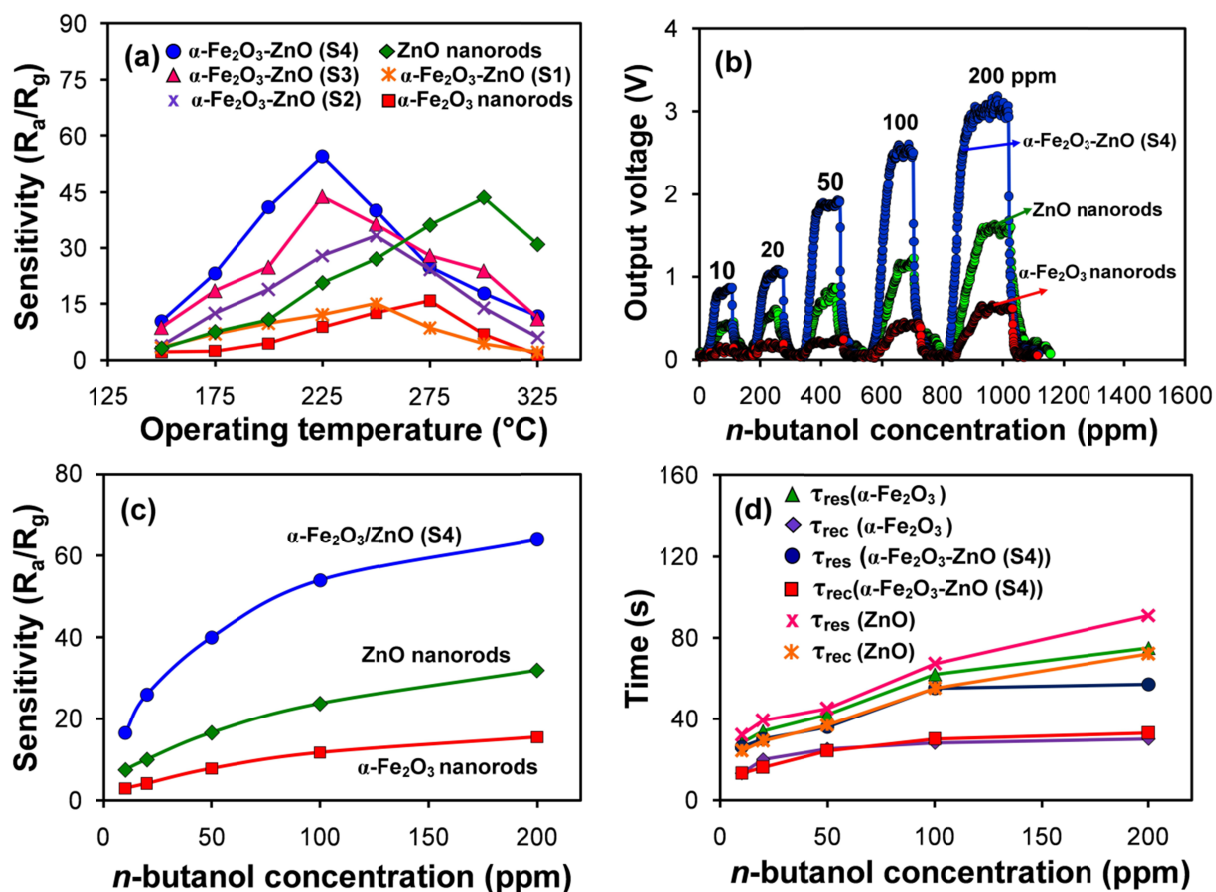
3.2 Gas-sensing performance

Fig. 8 (a) The sensitivity of the α-Fe$_2$O$_3$, ZnO and α-Fe$_2$O$_3$/ZnO (S1-S4) sensors toward 100 ppm of n-butanol as a function of the operating temperature, (b) dynamic response-recovery behaviors of the α-Fe$_2$O$_3$, ZnO and α-Fe$_2$O$_3$/ZnO sensors toward various concentrations of n-butanol at the optimum working temperature of 225 °C, (c) the sensitivity *vs.* concentration curves of the α-Fe$_2$O$_3$, ZnO and α-Fe$_2$O$_3$/ZnO (S4) sensors toward *n*-butanol at 225 °C, and (d) response-recovery time *vs.* n-butanol concentration plots of the three sensors at 225 °C.

As *n*-type semiconductors, α-Fe$_2$O$_3$ and ZnO nanostructures with various morphologies have been widely investigated as gas-sensing materials. However, the gas-sensing performance of a hetero-structure consisting of these two metal oxides toward volatile organic compounds (VOCs)

has been rarely investigated. In this study, we have used volatile n-butanol gas as the main target gas for detection, such that it can potentially be used in alcohol, wine and/or food analysis, e.g. for discriminating the type of alcohol in beers, wines and other alcoholic beverages.[20, 25] Moreover, n-butanol is often used in perfumes and fragrances, repellents, petroleum refineries and is frequently used as a solvent for paints, coatings, and natural and synthetic resins. Long-term exposure to n-butanol may be hazardous as it can act as a depressant to the central nervous system.[26] Therefore, it may be of interest to fabricate gas sensor materials with high sensitivity, selectivity, and stability toward n-butanol.

The operating temperature is one of the most important parameters affecting the sensitivity of a metal oxide gas sensor, as it governs the mobility of electrons and therefore the conductivity of the metal oxide material.[27, 28] Fig. 8a shows the changes in sensitivity of the six sensors toward 100 ppm of n-butanol with different operating temperatures. It can be noted that the sensitivity curves of these sensors show the typical bell-shape in the entire temperature range. Further observation of Fig. 8a reveals that α-Fe$_2$O$_3$/ZnO sensors containing higher quantities of Zn (samples S3 and S4) exhibit lower optimum operating temperatures of 225°C, as opposed to samples S1 and S2, which display highest sensitivities toward n-butanol gas at 250 °C. The maximum sensitivity values of the four α-Fe$_2$O$_3$/ZnO sensors toward 100 ppm of n-butanol are 15.1 (S1) at 250 °C, 33.3 (S2) at 250 °C, 43.8 at 225 °C, and 54.4 (S4) at 225 °C.

In comparison, the pristine α-Fe$_2$O$_3$ and ZnO sensors show the highest sensitivity toward n-butanol at much higher optimum operating temperatures of 275° and 330°C, respectively, which indicates the benefit of the ZnO modification. As sample S4 exhibit the highest sensitivity amongst the prepared α-Fe$_2$O$_3$/ZnO sensors, it is used as the main α-Fe$_2$O$_3$/ZnO sensor to

proceed with subsequent gas-sensing experiments. The dynamic response-recovery curves of the three sensors shown in Fig. 8b reveals the *n*-type sensing behaviors of all the fabricated sensors, whereby the output voltage of the sensors increases as the n-butanol gas is injected into the test chamber (with the highest increase observed for the α-Fe$_2$O$_3$/ZnO sensor) and subsequently decreases as the gas is removed.
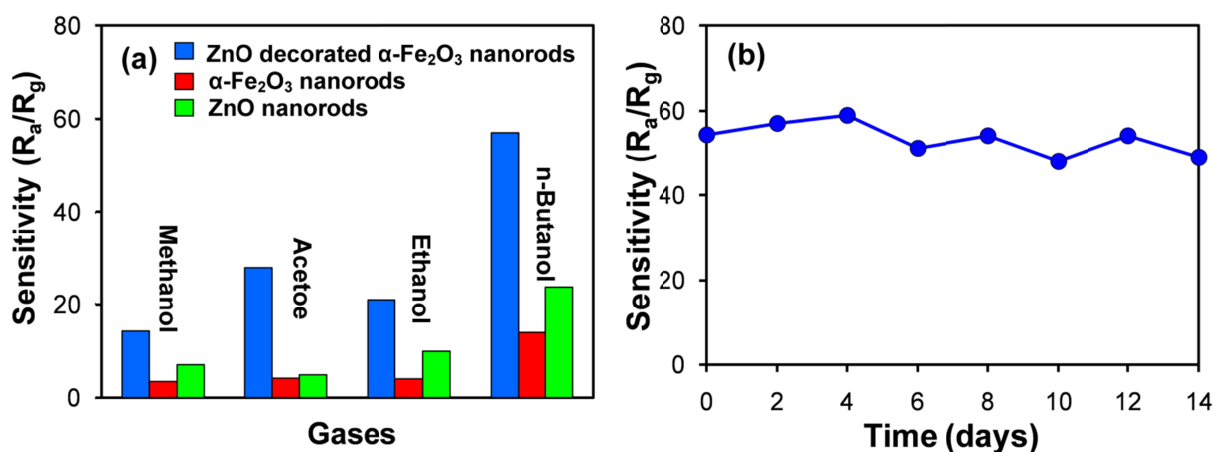

Fig. 9 (a) Selectivity tests of the α-Fe$_2$O$_3$, ZnO and α-Fe$_2$O$_3$/ZnO (S4) sensors toward various VOCs at 225 °C and (b) stability evaluation of the α-Fe$_2$O$_3$/ZnO sensor (S4) toward 100 ppm of n-butanol over a period of 14 days.

Fig. 8c compares the sensitivity of the pure α-Fe$_2$O$_3$ and ZnO, and α-Fe$_2$O$_3$/ZnO sensors (S4) as a function of n-butanol concentration at 225 °C. For all sensors, the trend is that the sensitivity initially rises quickly with increasing concentration before eventually reaching saturation at higher concentration levels. Furthermore, it can be observed from Fig. 8b that the α-Fe$_2$O$_3$/ZnO sensor (S4) shows approximately 4 times higher sensitivity compared to the pristine α-Fe$_2$O$_3$ sensor and 2.5 times higher sensitivity than the pristine ZnO sensor. These results clearly indicate the beneficial addition of ZnO NPs on the surfaces of α-Fe$_2$O$_3$ nanorods.

The dynamic response-recovery properties of the α-Fe$_2$O$_3$/ZnO sensor (S4) were also compared against the pure α-Fe$_2$O$_3$ and ZnO sensors, as depicted in Fig. 8d. The response times of the α-Fe$_2$O$_3$/ZnO sensor toward 10, 20, 50, 100, and 200 ppm of n-butanol are determined to be 26, 30, 36, 55 and 57 s, respectively. These are significantly faster than the response times of the pure α-Fe$_2$O$_3$ sensor (28, 34 52, 62 and 75 s, respectively) as well as those of the pure ZnO sensor (32, 39, 45, 67, and 91 s, respectively). Moreover, the recovery times of the α-Fe$_2$O$_3$/ZnO sensor toward 10-200 ppm of n-butanol are slightly faster than those of the pure α-Fe$_2$O$_3$ sensor and are approximately twice as fast compared to the pristine ZnO sensor.

Table 2 Comparison of the gas-sensing performance of various α-Fe$_2$O$_3$ or ZnO-based sensors toward 100 ppm of different VOCs.

Sensor Materials	Gases	T (°C)	*S*	References
	C$_4$H$_{10}$O	225	57	This work
ZnO-decorated α-Fe$_2$O$_3$	C$_3$H$_6$O	225	28	
	C$_2$H$_6$O	225	23	
α-Fe$_2$O$_3$/ZnO core/shell	C$_3$H$_6$O	200	12.5	[29]
	C$_2$H$_6$O	200	17.8	
α-Fe$_2$O$_3$/SnO$_2$ core/shell	C$_3$H$_6$O	320	2.3	[30]
	C$_2$H$_6$O	320	3	
TiO$_2$ decorated α-Fe$_2$O$_3$	C$_4$H$_{10}$O	370	27.5	[31]
	C$_2$H$_6$O	370	14.2	
Porous ZnO nanoflowers	C$_4$H$_{10}$O	320	25	[32]
α-Fe$_2$O$_3$ hollow spindles	C$_4$H$_{10}$O	180	14	[33]

Selectivity is another important parameter of a gas sensor. A good gas sensor can selectively detect a particular gas when it is exposed to an environment containing multiple gases with similar physicochemical properties. The selectivity of the α-Fe$_2$O$_3$, ZnO, and α-Fe$_2$O$_3$/ZnO (S4) sensor toward n-butanol was tested by comparing its sensitivity against other VOCs with nearly identical physicochemical properties, such as methanol, ethanol, and acetone. From Fig. 9a, it can be observed that the α-Fe$_2$O$_3$/ZnO sensor clearly exhibits the highest sensitivity toward volatile n-butanol gas, with $S = 54.4$ at a concentration of 100 ppm. This is around 2 to 5 times higher than the sensitivity toward other gases, indicating the excellent selectivity of the α-Fe$_2$O$_3$/ZnO sensor toward volatile n-butanol gas. In comparison, the selectivity of the pure α-Fe$_2$O$_3$ and ZnO sensors is not as satisfactory.

For practical applications, gas sensors not only need to exhibit high sensitivity and selectivity toward the target gases, but also good stability to ensure their long-term reliability. Fig. 9b shows the stability evaluation of the α-Fe$_2$O$_3$/ZnO sensor (S4) toward 100 ppm of n-butanol over a period of 2 weeks. It is obvious that the α-Fe$_2$O$_3$/ZnO sensor exhibits excellent stability toward n-butanol gas as the S values remain ≥ 50 during the 14 days of testing period. In comparison with previous studies, the as-prepared ZnO-decorated α-Fe$_2$O$_3$ nanorods display considerably enhanced sensitivity toward n-butanol compared to ZnO nanoflowers[32] and α-Fe$_2$O$_3$ hollow spindles at a much lower optimum operating temperature of 225 °C (Table 2).[33] Additionally, they also exhibit higher sensitivity toward other VOCs such as acetone and ethanol compared to previously reported α-Fe$_2$O$_3$/ZnO[29] and α-Fe$_2$O$_3$/SnO$_2$ core/shell nanocomposites,[30] as well as TiO$_2$-decorated α-Fe$_2$O$_3$ nanorods.[31]

3.4. Sensing mechanism

The sensing mechanism of *n*-type semiconducting metal oxides such as pure α-Fe$_2$O$_3$ and ZnO sensors can be explained in terms of the modulation of depletion layer by oxygen adsorption.[27] That is, when the pure α-Fe$_2$O$_3$ or ZnO sensor is exposed to air, oxygen molecules adsorb on the surfaces of the α-Fe$_2$O$_3$ or ZnO nanorods and ionize to O$^-$ or O^{2-} by capturing free electrons from the conduction band of α-Fe$_2$O$_3$ or ZnO. This reduces the free charge carrier (electron) concentration and leads to the formation of an electron depletion layer. However, when the n-butanol gas is injected into the testing chamber, the *n*-butanol molecules react with the adsorbed oxygen species on the surfaces of the α-Fe$_2$O$_3$ or ZnO nanorods. This in turn, releases the trapped electrons back into the conduction band of α-Fe$_2$O$_3$ or ZnO, which increases the free electron concentration, and ultimately decreases the resistance of the pure α-Fe$_2$O$_3$ or ZnO sensor.

From Fig. 8c, it is evident that the ZnO-decorated α-Fe$_2$O$_3$ nanorods exhibit 3-4 times higher sensitivity than pure α-Fe$_2$O$_3$ nanorods as well as twice the sensitivity of pure ZnO nanorods toward n-butanol gas. The significant improvement observed in the sensitivity of the α-Fe$_2$O$_3$ nanorods following the ZnO decoration can be attributed to the chemical and electronic sensitization induced by the ZnO NPs. Specifically, the presence of ZnO NPs on the surfaces of the α-Fe$_2$O$_3$ nanorods promotes the formation of a heterojunction barrier at the interface of the two metal oxides, which governs the electron transport properties of the nanocomposites. This is caused by the difference in their work functions (5.0 eV for ZnO and 5.88 eV for α-Fe$_2$O$_3$).[18] As the work function of α-Fe$_2$O$_3$ is higher than that of ZnO, the Fermi energy level of α-Fe$_2$O$_3$ is lower than that of ZnO. Therefore, a transfer of electrons will occur from the conduction band of α-Fe$_2$O$_3$ to that of ZnO to equalize the Fermi energy levels of the two oxides. Hence, an electron depletion layer is formed at the heterojunction of the two metal oxides, as depicted in Fig. 10b.
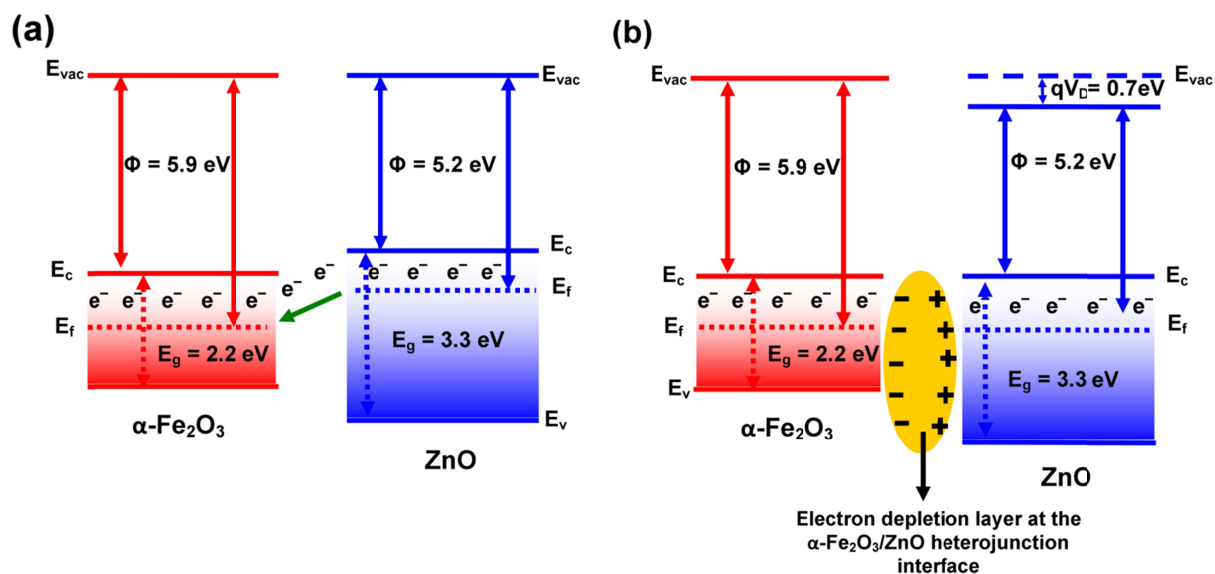
24

Fig. 10 Schematic diagram showing the possible band-gap arrangement of (a) α-Fe$_2$O$_3$ and ZnO and (b) α-Fe$_2$O$_3$/ZnO nanocomposites.

In the prepared ZnO-decorated α-Fe$_2$O$_3$ nanorods, the surfaces of the α-Fe$_2$O$_3$ nanorods are highly accessible for the adsorption of O$_2$ molecules as they are not completely enclosed by the ZnO NPs. Hence, when the α-Fe$_2$O$_3$/ZnO sensor is exposed to air, O$_2$ molecules can easily adsorb on the surfaces of both metal oxides and capture electrons from the conduction bands of both α-Fe$_2$O$_3$ and ZnO. This promotes the formation of depletion layers on the surfaces of both oxides, in addition to the depletion layer formed at the heterojunction interface of the two oxides. The presence of these multiple depletion layers significantly drains the free charge carriers from ZnO, making the as-prepared α-Fe$_2$O$_3$/ZnO sensor to be highly resistive compared to the pure α-Fe$_2$O$_3$ sensor. Then, when the α-Fe$_2$O$_3$/ZnO sensor is exposed to the n-butanol gas, the latter reacts with the richly available chemisorbed oxygen species (O$^-$ or O^{2-}) on the surfaces of both oxides and release a higher amount of trapped electrons (due to the presence of multiple depletion layers) compared to the case of pure α-Fe$_2$O$_3$ or ZnO sensor. Therefore, there is a

greater drop of resistance in the case of α-Fe$_2$O$_3$/ZnO sensor, which ultimately leads to the dramatic improvement observed in the sensitivity of the α-Fe$_2$O$_3$/ZnO sensor.

Aside from electronic sensitization, the introduction of the ZnO additive may also induce chemical sensitization by enhancing the catalytic properties of the base α-Fe$_2$O$_3$ material, similar to that observed in SnO$_2$-ZnO binary oxide.[34, 35] Specifically, the α-Fe$_2$O$_3$ component is capable of dehydrogenating butanol (C$_4$H$_{10}$O) to butanal (C$_4$H$_8$O) effectively, according to the equation:

$$C_4H_{10}O \rightarrow C_4H_9O^- + H^+ \rightarrow C_4H_8O + H_2 \tag{6}$$
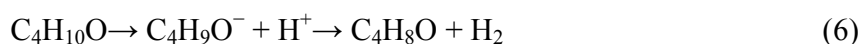
However, it may not be as effective in the catalytic breakdown of butanal, as described in Eq. (7) or (8) (depending on the adsorbed oxygen species present on the surfaces of the α-Fe$_2$O$_3$ nanorods):

$$2C_4H_8O + 22O^- \rightarrow 8CO_2 + 8H_2O + 22e^- \tag{7}$$

$$\text{or } 2C_4H_8O + 22O^{2-} \rightarrow 8CO_2 + 8H_2O + 44e^- \tag{8}$$
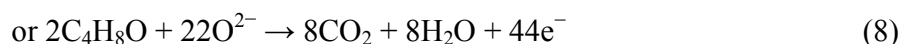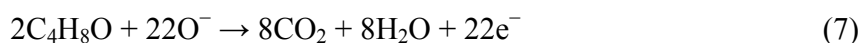
On the other hand, the ZnO component may be able to enhance the catalytic breakdown of butanal very effectively, as demonstrated in previous studies.[34, 35] Hence, the combination of these two materials can therefore effectively dehydrogenate butanol and subsequently catalyze the breakdown of butanal. The gas-sensing results obtained using the α-Fe$_2$O$_3$/ZnO nanocomposites clearly support this idea (Fig. 8c). This suggests that when the catalytic action of the metal oxide components complements each other, the gas-sensing performance can be improved.

4. Conclusions

A facile and efficient solvothermal method has been demonstrated for the synthesis of ZnO-decorated α-Fe$_2$O$_3$ nanorods under mild reaction conditions. The proposed method offers a

number of advantages including simple synthesis procedures and the lack of further calcination at high temperatures to achieve crystalline ZnO phase. The ZnO-decorated α-Fe$_2$O$_3$ nanorods show ~4 and 2 times higher sensitivity than pure α-Fe$_2$O$_3$ and ZnO nanorods, respectively, at a low optimum operating temperature of 225 °C. Additionally, they also exhibit faster response (reducing by up to 34 s) and recovery times (reducing by up to 39 s) to n-butanol gas compared to pure α-Fe$_2$O$_3$ and ZnO sensors, and a decrease of 50°-75°C in the optimum operating temperature. The improvement in the sensitivity of the α-Fe$_2$O$_3$/ZnO sensor is possibly caused by the existence of multiple depletion layers on the surfaces of the nanocomposites, which enhances the resistivity when exposed to the gas molecules compared to the pure α-Fe$_2$O$_3$ or ZnO sensor as well as due to the enhancement in the catalytic breakdown of n-butanol by the ZnO NPs. The simple synthesis strategy and the excellent gas-sensing properties of the ZnO-decorated α-Fe$_2$O$_3$ nanorods make them promising gas-sensing materials for the detection of volatile organic gases.

4. References

1.   J. S. Chen, C. M. Li, W. W. Zhou, Q. Y. Yan, L. A. Archer and X. W. Lou, *Nanoscale*, 2009, **1**, 280-285.

2.   Z. Zhang, C. Shao, X. Li, L. Zhang, H. Xue, C. Wang and Y. Liu, *J. Phys. Chem. C*, 2010, **114**, 7920-7925.

3. X. Xue, L. Xing, Y. Chen, S. Shi, Y. Wang and T. Wang, *J. Phys. Chem. C*, 2008, **112**, 12157-12160.

4. S. H. Hwang, J. Song, Y. Jung, O. Y. Kweon, H. Song and J. Jang, *Chem. Commun.*, 2011, **47**, 9164-9166.

5. Y. Liu, L. Yu, Y. Hu, C. Guo, F. Zhang and X. Wen Lou, *Nanoscale*, 2012, **4**, 183-187.

6. J. Kang, Q. Kuang, Z.-X. Xie and L.-S. Zheng, *J. Phys. Chem. C*, 2011, **115**, 7874-7879.

7. S. Zhang, F. Ren, W. Wu, J. Zhou, X. Xiao, L. Sun, Y. Liu and C. Jiang, *Phys. Chem. Chem. Phys.*, 2013, **15**, 8228-8236.

8. I.-S. Hwang, S.-J. Kim, J.-K. Choi, J. Choi, H. Ji, G.-T. Kim, G. Cao and J.-H. Lee, *Sens. Actuators B, Chem.*, 2010, **148**, 595-600.

9. W. Zhou, C. Cheng, J. Liu, Y. Y. Tay, J. Jiang, X. Jia, J. Zhang, H. Gong, H. H. Hng, T. Yu and H. J. Fan, *Adv. Funct. Mater.*, 2011, **21**, 2439-2445.

10. H. Wu, M. Xu, Y. Wang and G. Zheng, *Nano Res.*, 2013, **6**, 167-173.

11. Z. Sun, H. Yuan, Z. Liu, B. Han and X. Zhang, *Adv. Mater.*, 2005, **17**, 2993-2997.

12. X. Gou, G. Wang, J. Park, H. Liu and J. Yang, *Nanotechnology*, 2008, **19**, 125606.

13. G. Wang, X. Gou, J. Horvat and J. Park, *J. Phys. Chem. C*, 2008, **112**, 15220-15225.

14. X. Liu, Z. Chang, L. Luo, X. Lei, J. Liu and X. Sun, *J. Mater. Chem.*, 2012, **22**, 7232-7238.

15. X. Liu, J. Zhang, X. Guo, S. Wu and S. Wang, *Nanotechnology*, 2010, **21**, 095501.

16. Z. Lou, F. Li, J. Deng, L. Wang and T. Zhang, *ACS Appl. Mater. Interf.*, 2013, **5**, 12310-12316.

17. Y.-J. Chen, C.-L. Zhu, L.-J. Wang, P. Gao, M.-S. Cao and X.-L. Shi, *Nanotechnology*, 2009, **20**, 045502.

18.   J. Zhang, X. Liu, L. Wang, T. Yang, X. Guo, S. Wu, S. Wang and S. Zhang, *Nanotechnology*, 2011, **22**, 185501.

19.   W. Wu, S. Zhang, X. Xiao, J. Zhou, F. Ren, L. Sun and C. Jiang, *ACS Appl. Mater. Interf.*, 2012, **4**, 3602-3609.

20.   Y. V. Kaneti, J. Yue, X. Jiang and A. Yu, *J. Phys. Chem. C*, 2013, **117**, 13153-13162.

21.   S. Lian, E. Wang, Z. Kang, Y. Bai, L. Gao, M. Jiang, C. Hu and L. Xu, *Solid State Commun.*, 2004, **129**, 485-490.

22.   M. Niu, F. Huang, L. Cui, P. Huang, Y. Yu and Y. Wang, *ACS Nano*, 2010, **4**, 681-688.

23.   X. Li, H. Liu, J. Wang, X. Zhang and H. Cui, *Opt. Mater.*, 2004, **25**, 407-412.

24.   J. Yue, X. Jiang and A. Yu, *J. Phys. Chem. C*, 2012, **116**, 8145-8153.

25.   Y. V. Kaneti, Z. Zhang, J. Yue, X. Jiang and A. Yu, *J. Nanopart. Res.*, 2013, **15**, 1-15.

26.   A. D. Merritt and G. M. Tomkins, *J. Biol. Chem.*, 1959, **234**, 2778-2782.

27.   C. Wang, L. Yin, L. Zhang, D. Xiang and R. Gao, *Sensors*, 2010, **10**, 2088-2106.

28.   Y. V. Kaneti, Z. Zhang, J. Yue, Q. M. D. Zakaria, C. Chen, X. Jiang and A. Yu, *Phys. Chem. Chem. Phys*, 2014, DOI: 10.1039/C4CP01279H.

29.   S. Si, C. Li, X. Wang, Q. Peng and Y. Li, *Sens. Actuators, B*, 2006, **119**, 52-56.

30.   C. Yu-Jin, Z. Chun-Ling, W. Li-Jiao, G. Peng, C. Mao-Sheng and S. Xiao-Ling, *Nanotechnology*, 2009, **20**, 045502.

31.   Y. Wang, S. Wang, H. Zhang, X. Gao, J. Yang and L. Wang, *J. Mater. Chem. A*, 2014, **2**, 7935-7943.

32.   J. Huang, Y. Wu, C. Gu, M. Zhai, K. Yu, M. Yang and J. Liu, *Sens. Actuators, B*, 2010, **146**, 206-212.

33.   J. Huang, M. Yang, C. Gu, M. Zhai, Y. Sun and J. Liu, *Mater. Res. Bull.*, 2011, **46**, 1211-1218.

34.   B. P. J. de Lacy Costello, R. J. Ewen, P. R. H. Jones, N. M. Ratcliffe and R. K. M. Wat,

Sens. Actuators, B, 1999, **61**, 199-207.

35.   Y. Wang and B. H. Davis, *Appl. Catal. A*, 1999, **180**, 277-285.